Materials Science & Engineering A 718 (2018) 123–134

Contents lists available at ScienceDirect

Materials Science & Engineering A

journal homepage: www.elsevier.com/locate/msea

Impact of iron composition on the properties of an additively manufactured solid solution strengthened nickel base alloy

Z.R. Khayat[a], T.A. Palmer[b,c,*]

[a] Applied Research Laboratory, Pennsylvania State University, University Park, PA 16802, United States
[b] Department of Materials Science and Engineering, Pennsylvania State University, University Park, PA 16802, United States
[c] Department of Engineering Science and Mechanics, Pennsylvania State University, University Park, PA 16802, United States

ARTICLE INFO

Keywords:
Additive manufacturing
Inconel® 625
Directed energy deposition
Iron composition
Nickel base alloy
Hot isostatic pressing

ABSTRACT

The impact of changes in Fe content from 1 wt% to 4 wt% on the properties of additively manufactured (AM) Inconel® 625 fabricated using laser-based directed energy deposition (DED) is investigated in both the as deposited and post processed hot isostatically pressed (HIP) conditions. While similar solidification structures and microhardness values are observed, the low Fe content build displayed higher yield (520 MPa ± 12 MPa vs. 450 MPa ± 27 MPa) and tensile strengths (860 MPa ± 27 MPa vs. 753 MPa ± 25 MPa) and lower elongations (36% ± 5% vs. 44% ± 9%) in the as-deposited condition. Differences in mechanical properties are connected to differences in the grain size produced with the different Fe contents. In the as deposited condition, fine grains less than 500 μm in size with low aspect ratios were observed with the low Fe content, while large elongated grains in excess of 1 mm in length were observed with the high Fe content. After HIP, the yield strengths for both Fe contents decreased by 14%, while elongation increased similarly. On the other hand, tensile strengths after post processing changed by only 3%, which were correlated to higher levels of strain hardening for the higher Fe content. These differences in behavior can be attributed, in part, to changes in precipitate morphologies. After HIP post processing, the low Fe content build displayed Nb and Mo rich precipitates, while spherical Ti rich precipitates are present in the high Fe content build.

1. Introduction

Inconel® 625 is a solid-solution strengthened Ni-base alloy with high strength, outstanding corrosion resistance, and excellent fabricability. These properties make Inconel® 625 an attractive candidate for use in cryogenic and high temperature (> 980 °C) environments [1,2]. The versatility of this alloy system is derived from the combination of its primary alloying elements, which include Ni and Cr for high oxidation resistance, Mo for corrosion resistance, and Nb for stiffness. Table 1 provides a summary of the allowable composition limits for this alloy system [3]. While originally designed for high temperature environments characteristic of steam and gas turbines [4], its corrosion resistance has allowed its application space to be expanded into marine environments [5].

This alloy is widely used in the cast and wrought forms, but its good weldability also makes it an attractive material for clad overlays in steel structures and other applications where it can be used in an as-solidified condition [6–12]. In conventional arc welding and overlay processes, Inconel® 625 displays a columnar dendritic structure, with secondary phases forming in the interdendritic regions. These ordered secondary phases, which include various carbides (MC, M_6C, and $M_{23}C_6$) and Laves phase, are shown to have a detrimental effect on mechanical properties [8,13]. Laves phase, which is a brittle microconstituent, in particular, adversely affects ductility and acts as a crack initiation site [13–19]. Formation of the Laves phase is typically limited by controlling composition, with previous work directed at tightly controlling the Si, C, and Nb compositions. It has been observed that Laves phase formation was promoted [7,8] with high Si and low C compositions. Increased levels of Nb were also shown to increase secondary phase constituents as well as the solidification temperature range, resulting in increased crack susceptibility [8].

As shown in Table 1, there are rather large ranges of allowable alloying element compositions for several alloying elements in Inconel® 625. For example, Fe has a wide allowable range (0–5 wt%) [3], but the impact of large changes in the Fe content has not been specifically investigated. Most existing work dealing with changes in Fe content has been primarily directed at the dilution of the weld metal in clad overlays fabricated on steel structures [6–11]. In these applications, the weld metal becomes significantly enriched in Fe due to dilution from the carbon steel substrate, causing the Fe content to reach levels much

* Corresponding author at: Department of Materials Science and Engineering, Pennsylvania State University, University Park, PA 16802, United States.
E-mail address: tap103@psu.edu (T.A. Palmer).

https://doi.org/10.1016/j.msea.2018.01.112
Received 8 December 2017; Received in revised form 24 January 2018; Accepted 25 January 2018

Table 1
Summary of standard chemical compositions [3] and measurements of these compositions in low and high Fe content Inconel® 625 powder feedstock and as-deposited structures.

Element	Alloy Compositions (wt%)				
		Low Fe		High Fe	
	Standard	Powder	Deposit	Powder	Deposit
Ni	> 58.0	64.8	64.06	61.3	60.62
Cr	20.0 – 23.0	21.0	21.59	21.3	21.46
Fe	< 5.0	1.02	1.07	4.34	4.14
Mo	8.0 – 10.0	8.73	8.83	8.70	8.96
Nb	3.15 – 4.15	3.43	3.47	3.83	4.11
Si	< 0.50	0.37	0.39	0.035	0.051
Mn	< 0.50	0.31	0.28	0.010	0.085
C	< 0.10	0.008	0.009	0.005	0.006
Ti	< 0.40	0.019	0.033	0.19	0.21

higher than the allowable Fe range and altering the solidification path [6]. Dupont et al. found that the solidification temperature range in the deposited Inconel® 625 was suppressed because of the transfer of significant amounts of Fe to the overlay from the substrate [6].

Weldability and solidification studies of Inconel® 625 have been limited to the deposition of a small number of layers on both matching Inconel® 625 and steel substrate materials [6–11]. Additive manufacturing (AM) technologies, however, are capable of producing complex 3-dimensional components over a wide range of size scales [20–24]. Dilution of the deposited metal composition combined with the complex thermal cycles created by the continuous layer-by-layer melting and remelting are factors that influence the solidification path and final microstructure of the material [25]. When the deposition process is scaled, the governing process-structure-property relationships can change in unknown ways [26].

For larger scale applications, directed energy deposition (DED) AM processes are commonly used. In the case of Inconel® 625, several areas, including the role of powder feedstock size distributions [27], processing parameter control [28–30], microstructural impact [13,19,25,31,32], post processing [31], and mechanical properties [13,19,33] have been investigated. Additional AM work with the powder bed fusion (PBF) process, which is primarily used to fabricate smaller scale structures, has concentrated on microstructural characterization and the impact of hot isostatic pressing (HIP) on mechanical properties [34,35]. With the addition of this post processing step, the promotion of secondary phase formation is readily observed [16,36–39].

The Fe content in these previous AM studies was typically held constant at levels either below [19,25,27,40] or above [13,30,31,33] 3 wt%, which is at approximately the mid-level of the allowable composition range. The microstructures formed in these builds were characterized primarily by the presence of a $NbCr_2$ Laves phase, γ' (Ni_3Al), δ (Ni_3Nb), or one of several carbide phases. Little additional characterization of the impact of these different Fe levels on other microstructural and mechanical properties, though, is available.

In order to determine the impact of changes in the Fe content, laser-based DED Inconel® 625 builds were fabricated using powder feedstocks with 1 wt% and 4 wt% Fe levels. The resulting microstructural and mechanical properties were characterized in both the as deposited and post-processed HIP conditions. Even though the differences in Fe content are near the extremes of the allowable composition range, similar solidification microstructures, as characterized by secondary dendrite arm spacing (SDAS) and secondary phase volume fraction measurements, are observed along with similar microhardness levels across the height of the as-deposited builds. However, the lower Fe content builds displayed higher strength but lower elongation than the higher Fe content builds in the as deposited condition. These differences in as deposited mechanical properties correspond to differences in grain morphologies, with the low Fe content builds having a fine grain structure, while the high Fe content builds display large grains. After a post-process HIP treatment, the mechanical properties for both Fe contents decrease, but differences in the composition and morphology of secondary phases present in the structures lead to differences in the strain hardening behavior.

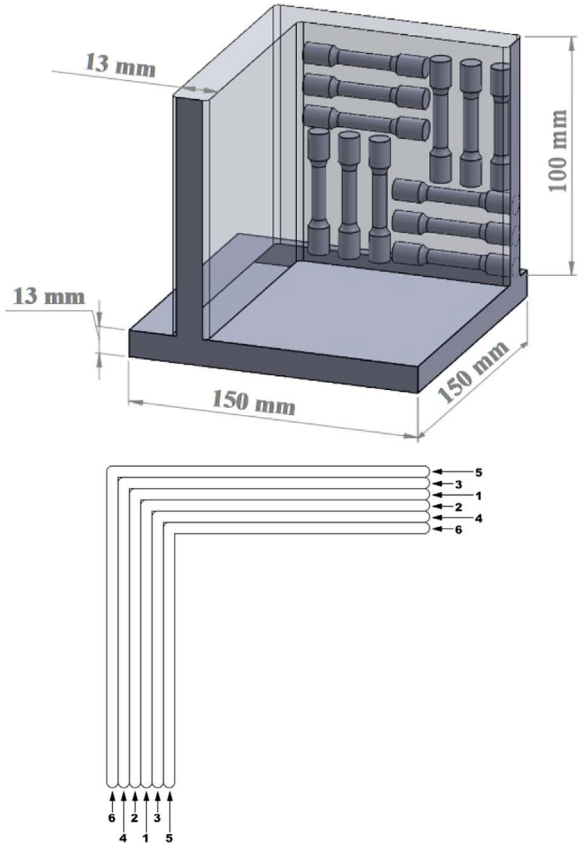

Fig. 1. Schematic diagram showing the solid model isometric view of the L shaped builds fabricated using a laser based DED AM process and the corresponding build path plan. Locations where tensile specimens were extracted from the fabricated structures are also shown. Longitudinal specimens are oriented parallel to the substrate, and transverse specimens are oriented perpendicularly.

2. Experimental

A series of L-shaped Inconel® 625 builds, schematically shown in Fig. 1, were fabricated using a laser based DED system on 150 mm × 150 mm × 13 mm thick Inconel® 625 substrates.[1] An IPG Photonics® YLR-12000 ytterbium fiber laser system operating at a near-infrared wavelength between 1070 and 1080 nm was used as the energy source. The laser was delivered through a 600 μm diameter fiber to a water-cooled copper reflective optics system, which consisted of a 49.5 mm diameter collimator with a 125 mm focal length lens and focusing optics with a focal length of 600 mm. The powder feedstock was delivered through a Powder Feed Dynamics Mark XV Precision Powder Feeder to a custom coaxial, four nozzle powder delivery system, with each nozzle having an orifice size of 2 mm and located 10 mm above the deposition surface. At this stand-off distance, the beam is operated in a defocused condition to ensure efficient powder consumption. The beam diameter was measured using a PRIMES® Focus Monitor and confirmed to be approximately 4 mm with a Gaussian energy density distribution [41].

Nitrogen atomized powder feedstocks[2] with a low Fe content (1 wt

[1] American Special Metals (Pompano Beach, FL).
[2] Carpenter Powder Products (Bridgeville, PA).

% Fe) and a high Fe content (4 wt% Fe) were obtained. The low Fe content powder was sieved to a size range between −100/+270 sieve sizes and the high Fe content powder was sieved to a size range between −120/+270 sieve sizes. Chemistries for the as received powder feedstock were measured at a certified testing laboratory[3] and are listed in Table 1. While these powder feedstocks were procured primarily to evaluate the role of changes in Fe content, other differences, primarily in Si and Ti, were also observed to coincide with the different Fe content. In the low Fe content powder feedstock, a higher level of Si (0.37 wt%) was present with a low level of Ti (0.019 wt%), while the high Fe content powder feedstock displayed a higher level of Ti (0.19 wt %) and a low level of Si (0.035 wt%).

Standard size, flow, and density characterization tests of the powder feedstock were also conducted, and the results are listed in Table 2. The volume based particle-size distribution was measured using a Mastersizer 3000 (software version V3.62)[4] laser diffraction particle size analyzer with a Hydro MV wet dispersion attachment. A small amount of dry powder was placed directly in small increments into the Hydro MV unit with a constant stirrer speed of 2390 RPM until an obscuration rate of 5% was achieved. The particle size distributions, including particle size at 10% (D_{10}), 50% (D_{50}), and 90% (D_{90}) of the volume distribution were calculated using refractive (1.86) and absorption (3.7) indices of dispersed droplets. Each powder feedstock was also characterized using traditional powder metallurgy techniques, including Hall flow rate (ASTM B213) [42], apparent density (ASTM B212) [43], tap density (ASTM B527) [44], and angle of repose (ASTM C1444) measurements [45].

All builds were fabricated using a laser power of 2000 W, a travel speed of 10.6 mm/s, and a mass flow rate of 16 g/min for the low Fe content builds and 14 g/min for the high Fe content builds. A hatch spacing of 2.54 mm was used for the low Fe content builds and was adjusted to 2.29 mm for high Fe content builds to eliminate surface irregularities and defects. The deposition chamber was purged using ultra high purity argon to an oxygen level less than 0.2 wt% prior to deposition. An argon gas flow rate of 2 L/min was used to deliver the powder, and additional argon shielding gas was coaxially delivered along the laser path. During the fabrication of the L-shaped structures, successive layers were deposited in an alternating pattern with the deposition head moving up .635 mm per pass [46], as shown in Fig. 1(b). Selected builds underwent a standard HIP treatment at a temperature of 1163 ± 25 °C and a pressure of 101 MPa for 14,400 s[5] All builds were inspected for internal pores and defects using an X-ray Computed Tomography (CT) system (GE, phoenix v|tome|x m 300) equipped with a 300 kV micro-focus x-ray source operated at a potential of 200 kV and current of 50 μA. A voxel size of 100 μm was used for all x-ray CT scans.

After fabrication and post processing, samples approximately 25 mm x 13 mm x 13 mm in size were extracted along the build height and used for metallurgical characterization. Samples were ground through a series of silicon carbide media up to P2000 ISO grit size, polished with 3 μm and 1 μm polycrystalline diamond suspension, and underwent a finish polish with 0.05 μm colloidal silica for 480 s. They were then immersed in a 10% oxalic acid solution and electrolytically etched at a potential of 2 V for a time of 2 s to prepare samples for optical microscopy, which was performed using a Nikon Epiphot microscope.

Solidification structures in Inconel® 625 contain primary and secondary dendrite arms and secondary phases, as shown in Fig. 2. Secondary dendrite arm spacing (SDAS) is a microstructural feature which can be quantitatively correlated with cooling rates during solidification [47]. SDAS was measured by locating at least five consecutive secondary dendrite arms and measuring the spacing between them. A minimum of 32 intercepted secondary dendrite arms were measured at selected locations along the build height using the ImageJ® (National Institutes of Health, Bethesda Maryland) software package to determine peak gray values which signified interdendritic regions. The length of the line across the secondary dendrite arms was determined by using the image pixels to micron conversion feature within the software [40]. Once the length of the line and the number of dendrites the line crossed were determined, the SDAS value, λ_2, was calculated using Eq. (1), where L is the length of the line and n is the number of intercepted dendrites.

$$\lambda_2 = \frac{L}{(n-1)} \quad (1)$$

Additional analysis was also used to determine the average secondary phase particle size and volume fraction. The threshold feature in the ImageJ® software was used to calculate the size and volume fraction of the secondary phases. In the threshold process, a standard optical micrograph is converted to an 8-bit black and white image. Microstructural features are then filtered so that only secondary phase particles remain. Once a threshold limit has been set, the size of each particle and overall volume fraction of second phase particles are calculated using a gray scale color analysis.

To identify small microstructural features and investigate the segregation of elements within the solidification structures, a scanning electron microscope (SEM) (FEI, Quanta 200) equipped with an energy dispersive X-ray spectroscopy (EDS) detector was used. An accelerating voltage of 20 kV, working distance of 10 mm, and a spot size of 6.8 mm was used to obtain the necessary signal count needed for quality EDS scans. The EDS composition maps were used to analyze the microsegregation of Nb and Mo to the interdendritic regions in the as deposited condition and the formation of precipitates in the HIP condition.

Since optical microscopy did not reveal grain boundaries in either the as deposited or HIP conditions, the grain morphology and size were visualized and measured using electron backscatter diffraction (EBSD). These EBSD measurements were made using a FEI Helios NanoLab 660 Field Emission Gun (FEG) SEM coupled with an Oxford Instruments NordlysMax^2 detector. A 70° pre-tilt specimen holder was used and was positioned towards the NordlysMax^2 detector in the processing chamber. EBSD specimens were initially prepared using the metallography techniques previously described for optical microscopy, followed by a final polish using a Buehler VibroMet Vibratory Polisher with 0.05 μm colloidal silica for 12 h. In cases where the grains were large enough to exceed the measurement space of a single EBSD scan, a series of up to 14 EBSD scans were stitched together in order to measure the grain size.

Measurements of the average grain size area, major axis, minor axis, and aspect ratio were made using tools available in the ImageJ® analysis software. The elliptical tool was utilized to make approximations of the columnar grain morphology. Within the measurement settings, the Area, Fit Ellipse, Shape Descriptors, Centroid, and Center of Mass

Table 2
Summary of particle size distributions and standard powder measurement s for the low Fe and high Fe content Inconel® 625 powder feedstocks.

	Low Fe	High Fe
Particle Size Distribution (μm)		
D_{10}	58.44 ± 0.67	45.18 ± 0.82
D_{50}	94.96 ± 0.09	69.92 ± 0.29
D_{90}	153.20 ± 0.45	108.0 ± 0
Powder Characterization		
Flow Rate, FR_H (sec)	13.9 ± 0	13.5 ± 0.06
Apparent Density (g/cm^3)	4.63 ± 0.01	4.35 ± 0
Tap Density (g/cm^3)	5.3 ± 0.01	5.1 ± 0
Angle of Repose (degrees)	27	30.5

[3] Luvak Laboratories (Boylston, MA).
[4] Malvern Instruments (Westborough, MA).
[5] Bodycote (Andover, MA).

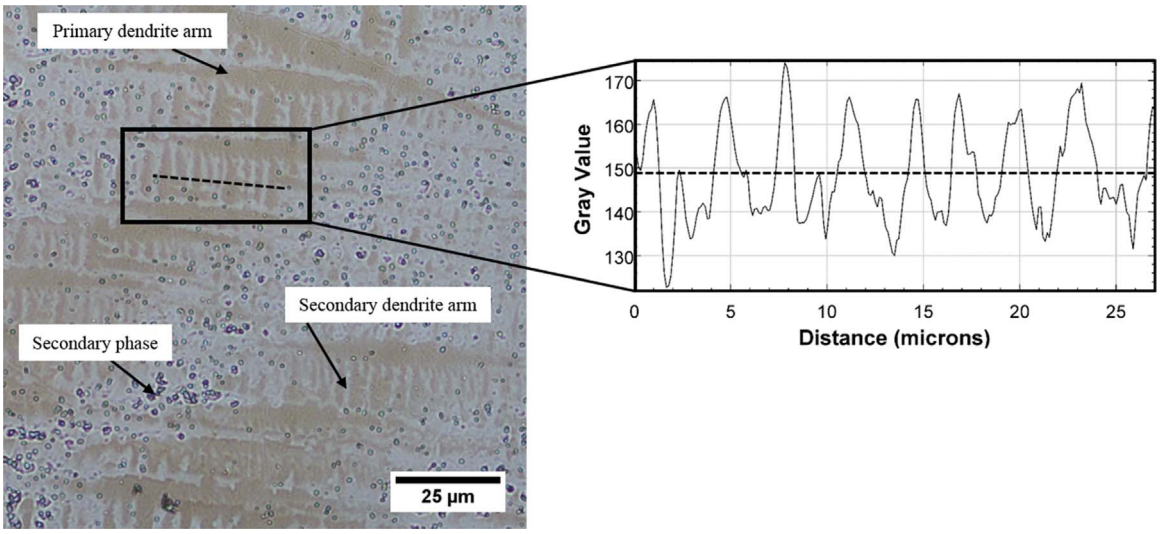

Fig. 2. Micrograph showing primary microstructural features, including primary and secondary dendrites and secondary phases, present in the as-deposited laser-based DED AM processed Inconel® 625 builds. A schematic illustration of the measurement of the secondary dendrite arm spacing (SDAS) is also shown, in which the peaks of the plot profile represent the interdendritic regions.

Identifier were engaged. In addition, the display label and overlay were also set to number the grains and mark where previous measurements were taken in order to avoid repeat measurements. The aspect ratio was calculated as the ratio of the major axis, a, to the minor axis, b [48]. An aspect ratio of 1 would signify that the grain is equiaxed. Averages and standard deviations were calculated and reported.

Microhardness testing was also conducted at selected locations along the build height using a Leco® M-400-G1 Vickers hardness tester to provide some correlation with the microstructural observations. Hardness indentations were spaced at 3 mm horizontal and vertical intervals to avoid any interactions between measurements. An applied load of 300 g with a dwell time of 5 s was used for all indentations. The average and standard deviation from the measurements taken at each height are reported.

Room temperature mechanical testing, with a strain rate of 0.005 min^{-1}, was conducted in accordance with ASTM E8 [49] at a certified testing laboratory.[6] Tensile specimens which met ASTM E8 standards [49] with a gauge diameter of 6.35 mm and a gauge length of 25.4 mm were extracted at selected locations and at different orientations, as shown in Fig. 1. The 0.2% offset yield strength and tensile strength were obtained from the resulting stress-strain curves, and the elongation was determined by measuring the gauge length before and after failure. In order to calculate the strain hardening exponent [50], the engineering stress (σ_e) and strain (ε_e) data were converted to the true stress (σ_t) and strain (ε_t) data by using Eqs. (2) and (3):

$$\varepsilon_t = \ln(1 + \varepsilon_e) \tag{2}$$

$$\sigma_t = \sigma_e(1 + \varepsilon_e) \tag{3}$$

True stress was plotted as a function of plastic true strain and the data points were fitted, using a power trendline, to the strain hardening power-law equation, as shown in Eq. (4):

$$\sigma_t = K\varepsilon_t^{\,n} \tag{4}$$

where σ_t is true stress, ε_t is plastic strain, K is the strength coefficient of the material, and n is the strain hardening exponent. From each build, twelve tensile specimens were extracted and tested. Strain hardening data from each test was compiled and averaged to determine the n-value for each build.

3. Results and discussion

3.1. Powder feedstock characterization

Powder feedstocks that meet the chemistry specifications for Inconel® 625 are typically considered equivalent and expected to behave in similar ways. However, the wide range of allowable compositions in the standards governing this alloy system can have unexpected effects on the powder feedstock and the resulting build. For example, a change in Fe content from 1 wt% to 4 wt% resulted in differences in the morphology of the powder feedstocks, as shown in Fig. 3. The low Fe content powder was generally spherical in shape and free of satellites, as shown in Fig. 3(a). On the other hand, the high Fe content powder, shown in Fig. 3(b), displayed a large number of satellites and fines, which resulted in an increase in particle roughness. In order to quantify the role that these differences in morphology played on the resulting powder properties, additional measurements were made to characterize powder size, flow characteristics, and interparticle friction.

Particle size distribution (PSD) curves obtained from a series of laser scattering measurements of both powder feedstocks are shown in Fig. 4, and the resulting D_{10}, D_{50}, and D_{90} are listed in Table 2. The low Fe content powder feedstock had a wider distribution and a larger average D_{50} of 95.0 ± 0.1 µm compared to 69.9 ± 0.3 µm for the high Fe content powder feedstock. Differences in the Gaussian distribution in the PSD curves shown in Fig. 4 for the low and high Fe content powder feedstocks can be attributed to the different sieving ranges used for the two powders.

While the low Fe content powder feedstock had an overall larger mean particle size, no measurable differences in the flowability, apparent density, and tap density, as listed in Table 2, were observed with the high Fe content powder. However, the angle of repose differed between the low and high Fe content powder feedstocks, with the low Fe content powder displaying an angle of repose value of 27° compared to an angle of repose value of 30.5° for the high Fe content feedstock. The change in angle of repose value can be attributed, in part, to the change in size of the powder feedstock particles and also the amount of fines in each powder feedstock [51]. High Fe content powder feedstock contains more fines, as shown in Fig. 3(b), and, as a consequence, leads to an increase in the interparticle friction [52], which affects the flowability of the powder particles and produces a higher angle of repose value.

[6] Westmoreland Mechanical Testing & Research, Inc. (Youngstown, PA).

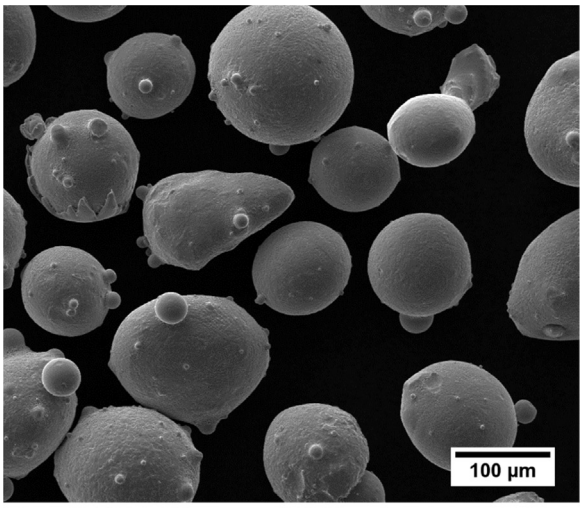

Fig. 3. (a&b): Micrographs showing the morphology of the (a) low and (b) high Fe Inconel® 625 nitrogen atomized powder.

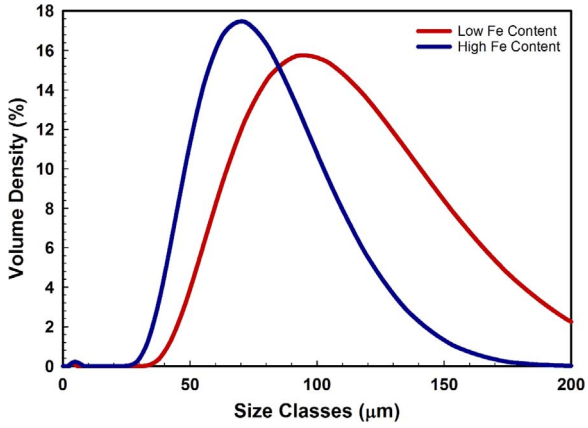

Fig. 4. Plot showing the particle size distribution curves for the low and high Fe content powder feedstocks.

3.2. Analysis of structures in the as deposited condition

Each powder feedstock was then used to fabricate a series of L-shaped structures in order to evaluate the impact of changes in powder feedstock composition on the as deposited build characteristics. Process-related defects within the build, such as lack of fusion defects, were first characterized using X-Ray CT scanning. In the builds fabricated using each powder feedstock, a minimal number of randomly distributed defects, indicative of lack of fusion between adjacent passes, were observed in each build [26]. Reported levels of porosity were below 0.005 vol%, which corresponded to an overall calculated volume of less 0.2 mm^3. Detected defects had a diameter of 0.05 ± 0.02 mm and sphericity of 0.70 ± 0.6.

An initial analysis of the as-deposited microstructures was performed to identify differences in the prominent microstructural features which might appear with changes in Fe content. Typical microstructures observed in the low and high Fe content builds are shown in Figs. 5 and 6, respectively. For both Fe contents at these magnifications, similar solidification microstructures, primarily comprised of primary and secondary dendrite structures interspersed with secondary phases,

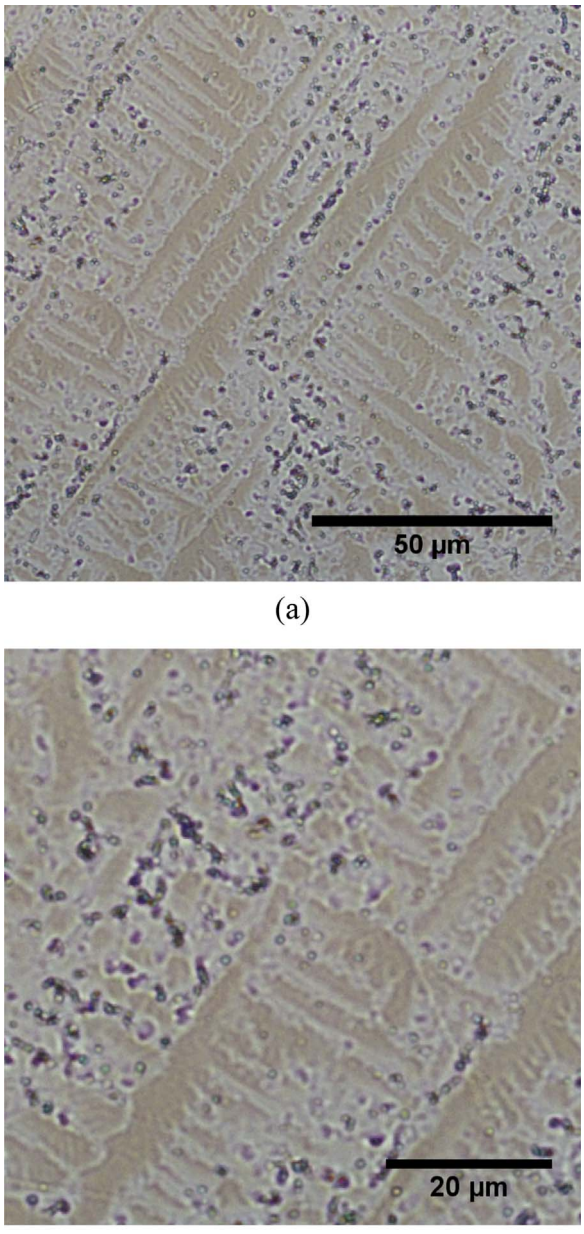

Fig. 5. (a&b): Optical micrographs of the solidification structure for the low Fe content as deposited builds at (a) low and (b) high magnifications highlighting the solidification structures and secondary phases.

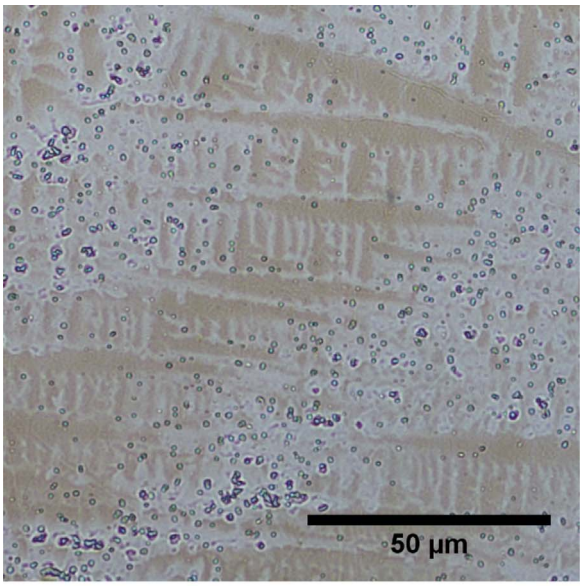

(a)

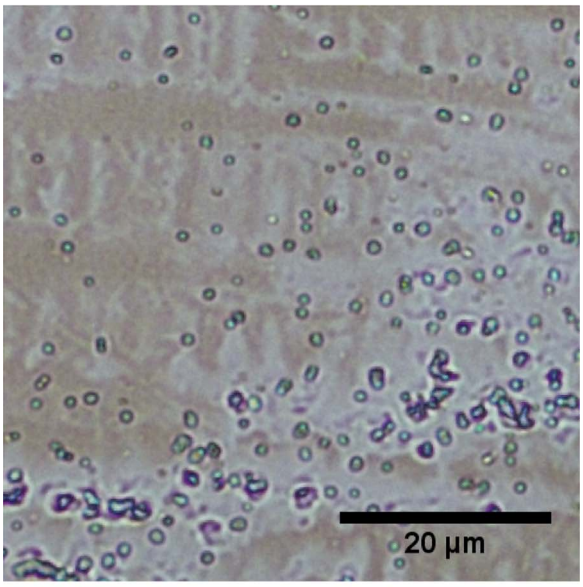

(b)

Fig. 6. (a&b): Optical micrographs of the solidification structure for the high Fe content as deposited builds at (a) low and (b) high magnifications highlighting the solidification structures and secondary phases.

were observed. Overall, however, there was very little change in the microstructural features observed in the builds fabricated using different Fe containing powder feedstocks. These similarities persist even at higher magnification, as shown in Figs. 5(b) and 6(b) for the low and high Fe content builds, respectively.

In order to quantify these similarities in microstructural features with changes in Fe content, additional measurements of the SDAS at specific locations were also performed. SDAS values have been quantitatively correlated with cooling rates for Ni-base alloys and can offer location specific information on how the cooling rate evolved throughout the height of the build [47]. In the as-deposited condition, the SDAS values displayed little change as a function of height and Fe content, as shown in Fig. 7. For example, average SDAS measurements made in the low Fe content build were 4.43 ± 0.22 µm, while those measured in the high Fe content build were 4.12 ± 0.38 µm. The

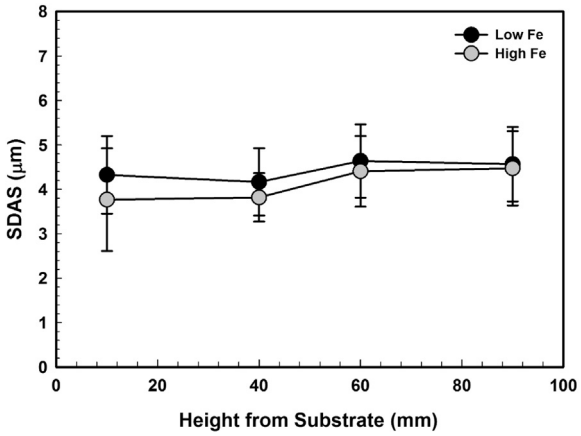

Fig. 7. Plot showing a comparison of the SDAS measurements across the height of the low and high Fe content builds.

similar SDAS measurements indicate that both samples experienced similar thermal conditions during AM fabrication and that the Fe content apparently had minimal, if any, impact on microstructural formation.

The size and volume fraction of second phase particles were also measured at selected locations along the height of each build. Second phase particles in builds fabricated with both Fe contents displayed blocky, irregularly shaped morphologies. Since the characteristics of the second phase particles did not change with increasing heights, the measured secondary phase particle size and volume fractions across the entire build heights were averaged and listed in Table 3. In the low Fe content build, the average volume fraction of secondary phases was 4.9 ± 0.4%, compared to 3.9 ± 0.5% for the high Fe content build. For the particle size measurements, the low Fe content build displayed an average particle size of 0.88 ± 0.21 µm, while the high Fe content build had an average particle size of 0.66 ± 0.29 µm. Based on these measurements, the low Fe content build had larger volume fractions and particle sizes than the high Fe content build, but the difference is not significant, making the role of Fe content on these secondary phases inconclusive.

When used in the as-deposited condition, the strength Inconel® 625 can be correlated to the SDAS values, with finer SDAS values giving higher microhardness values [53]. Because the SDAS measurements for the low and high Fe content builds are similar, it is expected that the microhardness measurements would be similar as well. In order to confirm this correlation, microhardness measurements were made across the height of each build to correspond with the microstructural measurements. The results are shown in Fig. 8, and similar microhardness values with no dependence on location are obtained for each Fe content. The average Vickers microhardness value for the low Fe content builds is 257 ± 9 HV and for the high Fe content builds is 258 ± 3 HV.

These similarities in microstructure and microhardness values for the low and high Fe content builds would normally be expected to lead to similarities in mechanical properties. Static mechanical testing was conducted on specimens extracted from the build at various heights and

Table 3
Summary of measurements of average size and volume fractions of secondary phases in low Fe and high Fe content builds in both the as-deposited and HIP conditions.

Fe Content and Build Condition	Average Particle Size (µm)	Volume % of Secondary Phase
Low Fe As deposited	0.88 ± 0.21	4.88 ± 0.41
HIP	1.36 ± 0.12	5.82 ± 0.83
High Fe As deposited	0.66 ± 0.29	3.86 ± 0.51
HIP	0.56 ± 0.08	4.50 ± 0.81

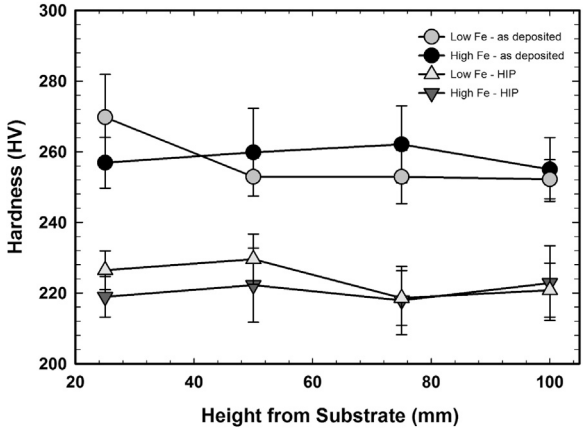

Fig. 8. Plot showing a comparison of the microhardness measurements as a function of build height for the low and high Fe content builds in the as-deposited and HIP conditions.

orientations, as shown in Fig. 1, and the results are listed in Table 4 with the corresponding engineering stress-strain curves shown in Fig. 9(a). Mechanical testing results did not show a dependence on height or orientation, but it is clear that the Fe content had a significant impact on the mechanical properties. Low Fe content specimens exhibited higher yield and tensile strengths but lower elongations. Specifically, the low Fe content specimens had an average yield strength of 520 MPa ± 12 MPa compared to an average yield strength of 450 MPa ± 27 MPa for high Fe content specimens. While low Fe content specimens had greater strengths, high Fe content specimens exhibited an average elongation value of 44 ± 9% compared to an average elongation of 36 ± 5% for the low Fe content specimens.

While the observed solidification microstructures within grains for the low and high Fe contents were similar, the differences in the mechanical properties must then be due to structural features not previously evaluated. In this case, differences in either the secondary phase composition and structure or grain size or a combination of the two can be responsible for these changes in mechanical properties. It is known that secondary phases, such as Laves phase and carbides, are observed in Inconel® 625 solidification structures produced through AM, cladding, and welding processes [12]. Previous solidification studies of Inconel® 625 suggested that increased amounts of Fe promoted Laves phase formation [6,15]. However, there is no strong supporting evidence here for increased Laves phase formation with higher Fe levels. In fact, the higher Fe levels produced lower amounts of secondary phases with smaller sizes than the low Fe contents.

A more in depth analysis to determine any differences in secondary phase formation was conducted using backscattered-electron (BSE) imaging along with EDS mapping, as shown in Fig. 10. Interdendritic regions for both the low and high Fe content builds were significantly

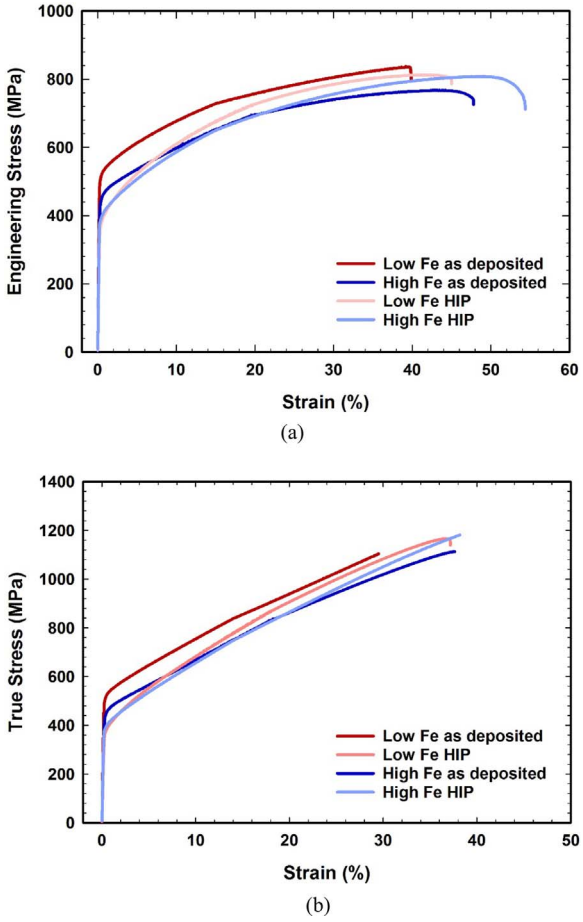

Fig. 9. (a&b): Representative (a) engineering stress-strain and (b) true stress-strain curves for low Fe and high Fe content Inconel® 625 builds.

enriched with Mo and Nb. Randomly dispersed throughout the matrix are remnants of additional alloying elements, such as Si in the low Fe content build and Ti in the high Fe content build, corresponding to the increased compositions of these alloying elements in the powder feedstock and build chemistries. However, similar segregation patterns are observed and do not appear to be responsible for these differences in mechanical properties.

Differences in the grain size with changes in Fe content, on the other hand, present a clear link with the differences in mechanical properties. The impact of Fe content on the size and morphology of the grains was investigated using EBSD techniques. Fig. 11 shows representative grain structures extracted from a location approximately 80 mm above the substrate in the low and high Fe content builds. Even though the

Table 4
Summary of mechanical property measurements made on low and high Fe content Inconel® 625 builds in the as deposited and HIP conditions.

Fe Content & Build Condition	Orientation	Number of Tensile Specimens Tested	Yield Strength (MPa)	UTS (MPa)	Elongation (%)	Strain Hardening Exponent
Low Fe As deposited	Longitudinal	6	531 ± 7	874 ± 25	32 ± 3	
	Transverse	6	508 ± 10	846 ± 24	40 ± 4	
	Average	**12**	**520 ± 12**	**860 ± 27**	**36 ± 5**	**0.33 ± 0.04**
HIP	Longitudinal	6	394 ± 17	841 ± 25	42 ± 4	
	Transverse	6	402 ± 15	848 ± 29	46 ± 4	
	Average	**12**	**398 ± 16**	**845 ± 26**	**44 ± 4**	**0.40 ± 0.01**
High Fe As deposited	Longitudinal	6	460 ± 35	763 ± 27	40 ± 7	
	Transverse	6	439 ± 6	743 ± 27	49 ± 8	
	Average	**12**	**450 ± 27**	**753 ± 25**	**44 ± 9**	**0.38 ± 0.02**
HIP	Longitudinal	6	383 ± 17	781 ± 28	48 ± 4	
	Transverse	6	387 ± 6	774 ± 16	55 ± 3	
	Average	**12**	**385 ± 12**	**778 ± 22**	**51 ± 5**	**0.42 ± 0.01**

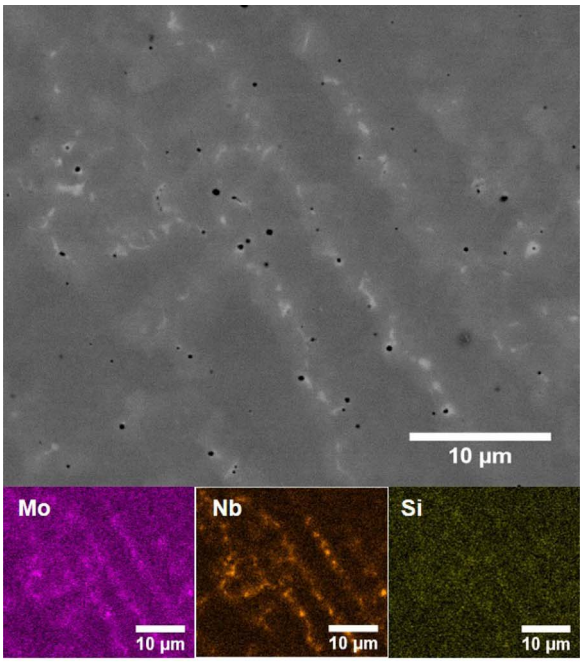

(a)

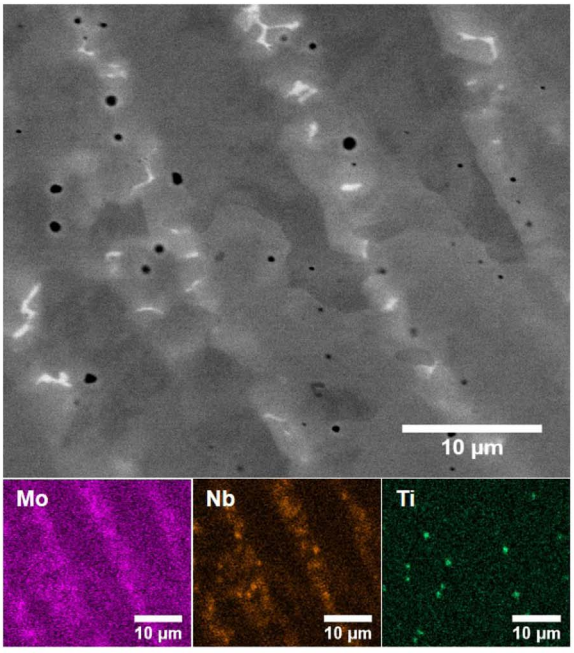

(b)

Fig. 10. (a&b): Microstructures and corresponding compositional maps of secondary phase structures in the (a) low Fe and (b) high Fe content builds in the as deposited condition. The bright regions are characteristics of Mo and Nb segregation, and the dark regions are Ti rich precipitates.

microstructures for each Fe content were dominated at higher magnifications by a dendritic structure, there are distinct differences in the grain size with changes in the Fe composition, with the low Fe content build displaying a much finer grain structure than the high Fe content build.

In order to quantify the resulting grain morphology and grain size, the average area, major and minor axis, and aspect ratio of the as deposited grains were measured, and the results are listed in Table 5. Low Fe content samples had columnar grains with an aspect ratio of 4.4 ± 2.6 and an average major axis length of 429 µm. High Fe content

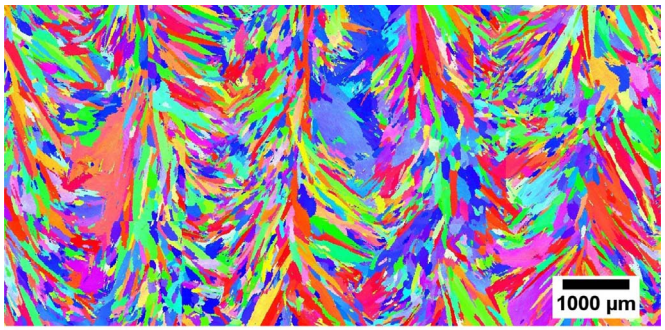

(a)

(b)

Fig. 11. Orientation contrast images of grain structures present at a location at 80 mm above the substrate in the as deposited condition of (a) low Fe and (b) high Fe content builds.

Table 5
Summary of grain size measurements obtained from the orientation contrast images for low and high Fe content Inconel® 625 builds.

	Low Fe		High Fe	
	As deposited	HIP	As deposited	HIP
Grain size and morphology measurements				
Mean of grain area (μm^2)	39600	37,000	441500	422,900
Average aspect ratio	4.4 ± 2.6	4.0 ± 2.2	5.5 ± 4.6	7.5 ± 5.8
a (µm)	429	390	1085	1468
b (µm)	108	106	280	254

builds had a similar aspect ratio of 5.5 ± 4.6 but a much larger major axis length of 1085 µm. The difference in grain size is better highlighted by measuring the average grain area. The low Fe content build displayed grains with an average area of 39,600 μm^2, but the average grain area in the high Fe content build grew to an area of 441,500 μm^2, which is approximately ten times larger. These significantly larger grain sizes in the high Fe content build can be directly correlated with decreased strength and increased ductility in the as deposited condition.

3.3. Impact of post processing

A post processing HIP treatment is primarily applied to AM structures to reduce internal porosity and other process related defects, such as those originating from lack of fusion [22]. For a range of materials, including Ti-6Al-4V and 316 L stainless steel, mechanical properties of wall structures fabricated using a laser based DED process have been shown to decrease after HIP post processing [13,23,35,46]. In order to determine the impact of HIP post-processing on AM fabricated Inconel® 625 builds, as-deposited low Fe content and high Fe content Inconel® 625 builds were subjected to a standard HIP cycle. X-ray CT scanning of the HIP structures was used to determine if any remaining defects could be detected. The analysis showed that no detectable levels of porosity

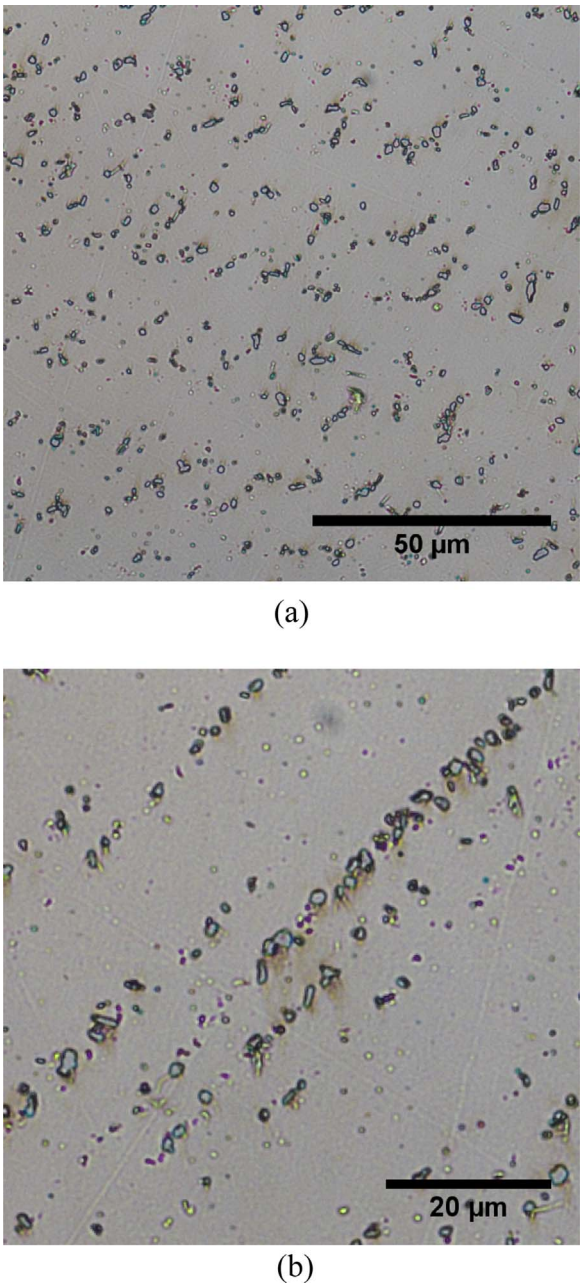

Fig. 12. (a&b): Optical micrographs showing the representative microstructures at (a) low and (b) high magnification in HIP post processed low Fe content builds.

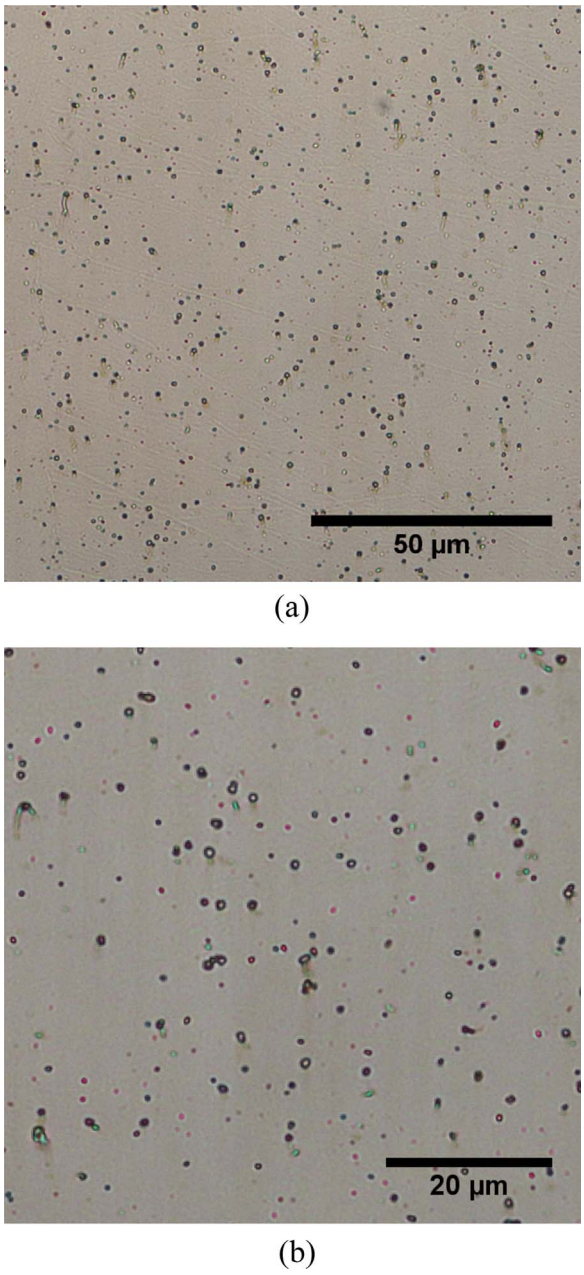

Fig. 13. (a&b): Fig. 12(a&b): Optical micrographs showing the representative microstructures at (a) low and (b) high magnification in HIP post processed low Fe content builds.

remained in either the low Fe content or high Fe content HIP builds, allowing for the properties of the HIP microstructures to be characterized independent of process-related defects.

The impact of the HIP post-processing cycle on the as-deposited microstructures is shown in Figs. 12 and 13 for the low Fe and high Fe content builds, respectively. Primary and secondary dendrite arms, which are prevalent in the solidification structure in the as-deposited condition, are not observed in the HIP microstructure. Rather, secondary phases with similar spherical and irregular blocky shaped morphologies as those observed in the as-deposited condition are readily distributed throughout the matrix material with no discernible solidification sub-structure. Table 3 lists the average particle size and volume fraction of the secondary phase. While there are no significant differences in the volume fractions of the secondary phases for each Fe content build, the particle size for the low Fe content HIP structure increases slightly from the as-deposited condition to an average size of $1.36 \pm 0.12\,\mu m$. On the other hand, the particle size for the high Fe content HIP structures remains the same as the as-deposited condition with an average size of $0.56 \pm 0.08\,\mu m$.

In order to compare the impact of the HIP post-processing cycle on the localized structure and properties, a series of microhardness measurements were made across the height of the low Fe and high Fe content builds. These microhardness measurements are plotted as a function of height and compared to the results obtained in the as-deposited condition for both Fe contents in Fig. 8. Similar to the as-deposited condition, changes in Fe content and build height location have no impact on the microhardness measurements in the HIP post-processed condition. For example, the average Vickers microhardness value for the low Fe content HIP structure was 224 ± 5 HV and 220 ± 2 HV for the high Fe content HIP structure. On the other hand, the HIP structures displayed a rather significant decrease of 13% in microhardness levels when compared to the as-deposited condition.

With this observed change in microhardness levels after HIP post-processing, the corresponding impact on the mechanical properties was further explored. Static mechanical tests similar to those performed on the as-deposited structures were conducted on samples extracted from selected locations and orientations in the low Fe and high Fe content HIP structures. The mechanical property results are reported in Table 4. Similar to the decrease in microhardness measurements after HIP post-processing, yield strengths in the HIP condition significantly decreased from that observed in the as-deposited condition for both Fe contents. For example, the yield strength of the specimens extracted from the low Fe content builds decreased from a yield strength of 520 MPa ± 12 MPa in the as-deposited condition to 398 MPa ± 16 MPa in the HIP condition. In the high Fe content builds, a similar decrease was observed, with the yield strength decreasing from a level of 450 MPa ± 27 MPa in the as-deposited condition to 385 MPa ± 12 MPa in the HIP condition. The magnitude of the decrease in yield strength between the as deposited and HIP conditions differed with changes in Fe content, with the decrease being 122 MPa for the low Fe content and 65 MPa for the high Fe content. In the case of the ductility, the addition of a HIP post processing cycle increased the elongation for both Fe contents over the as-deposited results, with the average elongation in the low Fe content HIP structure increasing to 44 ± 4% and to 51 ± 5% in the high Fe content HIP structure.

It was shown in the as deposited condition that the high Fe content build displayed a much coarser grain structure than the low Fe content build, which, in turn, was responsible for the decreased yield and tensile strengths. With the addition of a post-processing HIP cycle, changes in the grain structure as well as increases in the grain size would be expected to further decrease the strength for both Fe compositions. Columnar grains, similar to those observed in the as deposited builds, were also observed in both Fe compositions in the HIP condition, as shown in Fig. 15. Even with the addition of the high temperature HIP post-processing treatment, though, there is little change in the grain size and shape from that observed in the as deposited condition for both Fe contents, as shown in the grain size and morphology measurements listed in Table 5. For example, the average aspect ratio for low Fe content samples was 4.0 ± 2.2 with a major axis of 390 μm, and the average aspect ratio for high Fe content samples was 7.5 ± 5.8 with a major axis of 1468 μm.

The lower level of grain coarsening observed between the as-deposited and HIP conditions for both the low and high Fe content builds does not fully account for the differences in mechanical properties. In particular, the UTS values for the high Fe content build actually increased from 753 MPa ± 25 MPa in the as deposited condition to 778 MPa ± 22 MPa in the HIP condition. While the UTS values for low Fe content builds appear to be governed by the grain size, which does not significantly change between the as-deposited and HIP conditions, there are apparently other mechanisms driving the increase in UTS for the high Fe content builds.

This difference in UTS in the high Fe content builds can be correlated with the strain hardening behavior during plastic deformation. In order to quantify the strain hardening behavior for both the as-deposited and HIP conditions, the engineering stress-strain curves obtained during mechanical testing were converted to true stress-strain curves, which are shown in Fig. 9(b), and the corresponding strain hardening exponents are listed in Table 4. For both the low and high Fe content builds, the strain hardening exponents increased after HIP, with the low Fe content builds displaying strain hardening exponents that increase from 0.33 ± 0.04 in the as-deposited condition to 0.40 ± 0.01 in the HIP condition and the high Fe content builds increasing from 0.38 ± 0.02–0.42 ± 0.01. Overall, however, the high Fe content builds displayed higher strain hardening exponents than the low Fe content builds.

Since grain size showed little change between the as deposited and HIP conditions these differences in both strength and strain hardening behavior can be traced to differences in the characteristics of the

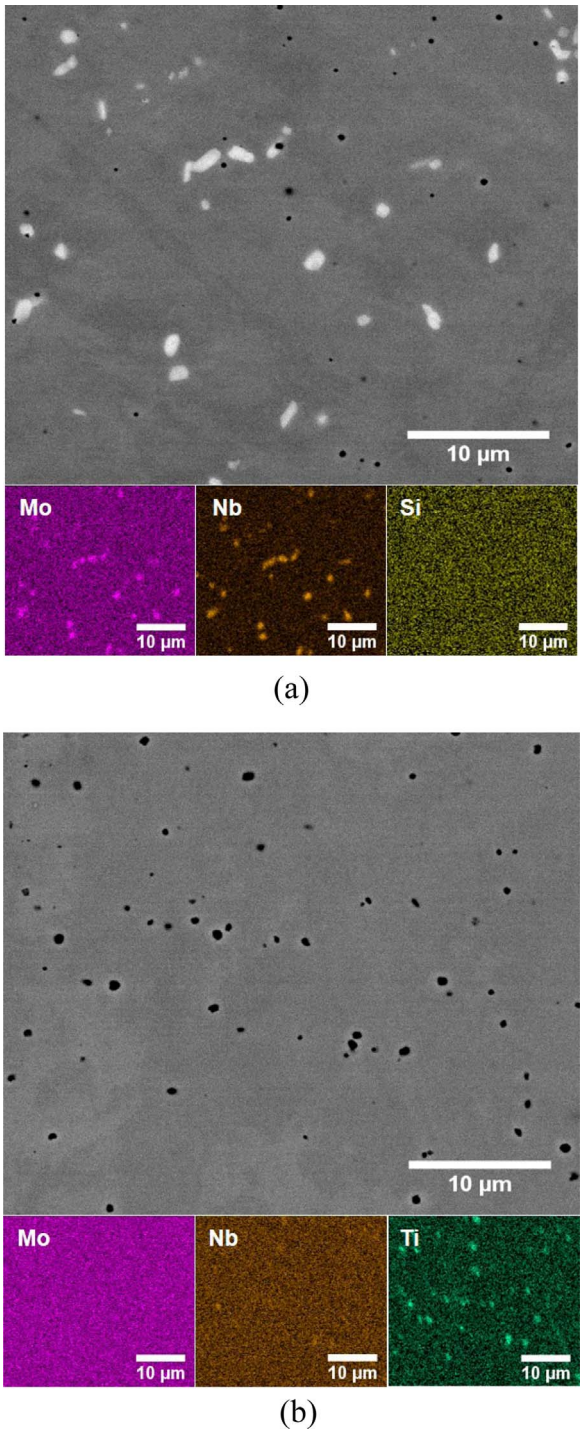

Fig. 14. Microstructures and corresponding compositional maps of secondary phase structures in the (a) low Fe and (b) high Fe content builds in the HIP condition detailing the (a) formation of Mo and Nb rich precipitates and the (b) dissolution of Mo and Nb in the matrix and the formation of Ti-rich precipitates.

secondary phases which exist in the low Fe and high Fe content builds. A more in depth examination of the composition of the secondary phases which exist in the HIP condition for the low and high Fe content builds are shown in Fig. 14(a) and (b), respectively. In the low Fe content HIP condition, the high degree of Mo and Nb segregation observed in the as deposited condition persisted in the HIP condition, with Mo and Nb rich precipitates with an average diameter of 0.84 ± 0.22 μm dominating the HIP microstructure, as shown in Fig. 15. In the high Fe content HIP condition, however, the Mo and Nb

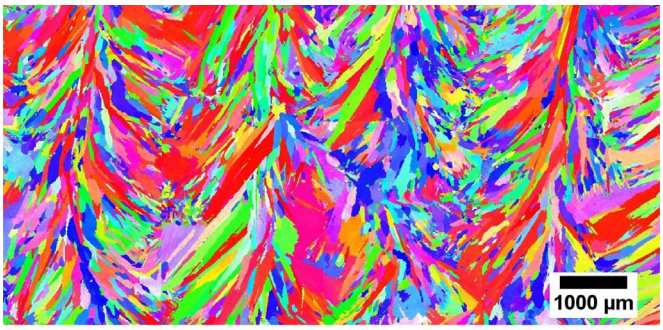

(a)

(b)

Fig. 15. Orientation contrast images of grain structures present at a location at 80 mm above the substrate in the HIP post-processed condition of (a) low Fe and (b) high Fe content builds.

segregation observed in the as-deposited condition disappeared after HIP post processing, with the Mo and Nb going into solution in the matrix. Small Ti rich precipitates with an average diameter of 0.5 ± 0.2 μm are prominent in the HIP microstructure. These Ti-rich precipitates originate from the increased Ti content in the high Fe content powder feedstock to a level of 0.19 wt%, which is an order of magnitude higher than that present in the low Fe content build (0.019 wt%).

4. Summary and conclusions

Allowable composition ranges for alloying elements, such as Cr, Mo, and Fe, in Inconel® 625 can be rather broad, with Fe ranging from 0 to 5 wt%. While these wide alloying element composition ranges do not impact wrought alloy properties, the changes in processing conditions introduced by laser-based DED AM processes can amplify the impact of these differences, particularly in the case of Fe. A change in Fe content from 1 wt% to 4 wt% is found to impact the grain size and secondary phase morphologies in both as deposited and HIP post-processed laser-based DED AM Inconel® 625. These changes in structure, primarily in grain size, lead to significant differences in the mechanical properties in the as-deposited condition. Lower Fe contents are shown to produce higher strengths and lower elongations as well as finer grain sizes than the higher Fe content, whose structure is dominated by large grains. HIP post processing produced lower microhardness values and yield strengths for both Fe contents. However, the higher Fe content build displayed an increased strain hardening response, resulting in an increase in UTS. Since there is little change in the grain structure between the as-deposited and HIP structures, changes in the composition and morphology of the secondary phases present in each microstructure contribute to this change in performance. The primary precipitates for low Fe content were rich in Nb and Mo, while the high Fe content build was dominated by precipitates rich in Ti, as the Nb and Mo appeared to go into solid solution in the matrix with HIP post-processing.

- Changes in Fe composition from 1 wt% to 4 wt%, which correspond to the extremes of the allowable composition range, in laser based DED AM processed Inconel® 625 produced similar SDAS and secondary phase features as well as microhardness measurements across the height of as-deposited structures.
- Even though similar microstructures are present in the builds fabricated with different Fe contents, significant differences in mechanical properties are observed. The low Fe content (1 wt%) build displayed higher yield (520 MPa ± 12 MPa vs. 450 MPa ± 27 MPa) and tensile strengths (860 MPa ± 27 MPa vs. 753 MPa ± 25 MPa) and lower elongations (36% ± 5% vs. 44% ± 9%) than the high Fe content (4 wt%). Changes in location or orientation had no impact on the mechanical properties for either Fe content.
- Differences in the mechanical properties for the different Fe contents in the as-deposited condition can be correlated with the impact of Fe content on grain size. Low Fe content produced smaller grains with low aspect ratios, while large elongated grains in excess of 1 mm in length were observed with the high Fe content.
- The addition of a post-processing HIP treatment on AM structures produced only minor changes in the grain size, but the addition of this post-processing treatment resulted in a 14% decrease in yield strength and a similar increase in elongation for both Fe contents. UTS values, though, displayed only a 3% change due to increasing levels of strain hardening observed with the higher Fe content.
- The secondary phase morphology observed in the HIP post-processed builds differed with the Fe content. Nb and Mo rich precipitates dominate the low Fe content structure, while spherical Ti rich precipitates, originating from an increased Ti content in the high Fe content powder feedstock, are present in the high Fe content builds.

Acknowledgements

The material is based upon work supported under the Department of Energy EERE FOA-0001006. We also acknowledge the Center for Innovative Materials Processing through Direct Digital Deposition (CIMP-3D) for their use of equipment, Mr. Jay Tressler for fabrication of the structures and general processing support, Mr. Ed Good for use of his metallurgical laboratory, and Mr. Andrew Iams for assistance with acquiring EBSD scans.

References

[1] C. Thomas, P. Tait, The performance of Alloy 625 in long-term intermediate temperature applications, Int. J. Press. Vessel. Pip. 59 (1994) 41–49, http://dx.doi.org/10.1016/0308-0161(94)90140-6.
[2] Inconel Alloy 625, Spec. Met. Corp, 2013.
[3] ASTM B705 − 05, Standard specification for nickel-alloy (UNS N06625, N06219 and N08825) welded pipe, ASTM Int. 5 (2015) 3–5, http://dx.doi.org/10.1520/B0705-05R09.
[4] J.N. DuPont, J.C. Lippold, S.D. Kiser, Welding Metallurgy and Weldability of Nickel-Base Alloys, John Wiley & Sons, Inc, Hoboken, New Jersey, 2009.
[5] K.P. Cooper, P. Slebodnick, E.D. Thomas, Seawater corrosion behavior of laser surface modified Inconel 625 alloy, Mater. Sci. Eng. A. 206 (1996) 138–149, http://dx.doi.org/10.1016/0921-5093(95)10013-X.
[6] J.N. DuPont, Solidification of an alloy 625 weld overlay, Metall. Mater. Trans. A. 27 (1996) 3612–3620, http://dx.doi.org/10.1007/BF02595452.
[7] M.J. Cieslak, T.J. Headley, A.D. Romig, T. Kollie, A melting and solidification study of alloy 625, Metall. Trans. A. 19 (1988) 2319–2331, http://dx.doi.org/10.1007/BF02645056.
[8] M.J. Cieslak, The welding and solidification metallurgy of alloy 625, Weld. J. 70 (1991) 49–56.
[9] J.C. Heigel, P. Michaleris, T.A. Palmer, In situ monitoring and characterization of distortion during laser cladding of Inconel® 625, J. Mater. Process. Technol. 220 (2015) 135–145, http://dx.doi.org/10.1016/j.jmatprotec.2014.12.029.
[10] J.C. Heigel, P. Michaleris, T.A. Palmer, Measurement of forced surface convection in directed energy deposition additive manufacturing, Proc. Inst. Mech. Eng. Part B J. Eng. Manuf. 230 (2016) 1295–1308, http://dx.doi.org/10.1177/0954405415599928.
[11] J.C. Heigel, M.F. Gouge, P. Michaleris, T.A. Palmer, Selection of powder or wire feedstock material for the laser cladding of Inconel 625, J. Mater. Process. Technol. 231 (2016) 357–365, http://dx.doi.org/10.1016/j.jmatprotec.2016.01.004.

[12] C.C. Silva, H.C. De Miranda, M.F. Motta, J.P. Farias, C.R.M. Afonso, A.J. Ramirez, New insight on the solidification path of an alloy 625 weld overlay, J. Mater. Res. Technol. 2 (2013) 228–237, http://dx.doi.org/10.1016/j.jmrt.2013.02.008.
[13] L.E. Murr, E. Martinez, S.M. Gaytan, D.A. Ramirez, B.I. MacHado, P.W. Shindo, J.L. Martinez, F. Medina, J. Wooten, D. Ciscel, U. Ackelid, R.B. Wicker, Microstructural architecture, microstructures, and mechanical properties for a nickel-base superalloy fabricated by electron beam melting, Metall. Mater. Trans. A Phys. Metall. Mater. Sci. 42 (2011) 3491–3508, http://dx.doi.org/10.1007/s11661-011-0748-2.
[14] M.J. Cieslak, G.A. Knorovsky, T.J. Headley, A.D. Romig, The use of new PHACOMP in understanding the solidification microstructure of nickel base alloy weld metal, Metall. Trans. A. 17 (1986) 2107–2116, http://dx.doi.org/10.1007/BF02645909.
[15] S. Floreen, G.E. Fuchs, W.J. Yang, The metallurgy of alloy 625, Superalloys (1994) 13–37, http://dx.doi.org/10.7449/1994/Superalloys_1994_13_37.
[16] G.D. Janaki Ram, A. Venugopal Reddy, K. Prasad Rao, G. Madhusudhan Reddy, Control of laves phase in inconel 718 GTA welds with current pulsing, Sci. Technol. Weld. Join. 9 (2004) 390–398, http://dx.doi.org/10.1179/136217104225021788.
[17] P. Nie, O.A. Ojo, Z. Li, Numerical modeling of microstructure evolution during laser additive manufacturing of a nickel-based superalloy, Acta Mater. 77 (2014) 85–95, http://dx.doi.org/10.1016/j.actamat.2014.05.039.
[18] K.-M. Chang, H.-J. Lai, J.-Y. Hwang, Existence of laves phase in Nb-hardened superalloys, superalloys 718, 625, 706 Var. Deriv. (1994) 683–694, http://dx.doi.org/10.7449/1994/Superalloys_1994_683_694.
[19] M. Rombouts, G. Maes, M. Mertens, W. Hendrix, Laser metal deposition of Inconel 625: microstructure and mechanical properties, J. Laser Appl. 24 (2012) 52007, http://dx.doi.org/10.2351/1.4757717.
[20] W.E. Frazier, Metal additive manufacturing: a review, J. Mater. Eng. Perform. 23 (2014) 1917–1928, http://dx.doi.org/10.1007/s11665-014-0958-z.
[21] D.D. Gu, W. Meiners, K. Wissenbach, R. Poprawe, Laser additive manufacturing of metallic components: materials, processes and mechanisms, Int. Mater. Rev. (2012), http://dx.doi.org/10.1179/1743280411Y.0000000014.
[22] W.J. Sames, F.A. List, S. Pannala, R.R. Dehoff, S.S. Babu, The metallurgy and processing science of metal additive manufacturing, Int. Mater. Rev. 61 (2016) 315–360, http://dx.doi.org/10.1080/09506608.2015.1116649.
[23] J.J. Lewandowski, M. Seifi, Metal additive manufacturing: a review of mechanical properties, Annu. Rev. Mater. Res. 46 (2016) 151–186, http://dx.doi.org/10.1146/annurev-matsci-070115-032024.
[24] T. DebRoy, H.L. Wei, J.S. Zuback, T. Mukherjee, J.W. Elmer, J.O. Milewski, A.M. Beese, A. Wilson-Heid, A. De, W. Zhang, Additive manufacturing of metallic components – process, structure and properties, Prog. Mater. Sci. 92 (2018) 112–224, http://dx.doi.org/10.1016/j.pmatsci.2017.10.001.
[25] G.P. Dinda, A.K. Dasgupta, J. Mazumder, Laser aided direct metal deposition of Inconel 625 superalloy: microstructural evolution and thermal stability, Mater. Sci. Eng. A. (2009), http://dx.doi.org/10.1016/j.msea.2009.01.009.
[26] T. Mukherjee, J.S. Zuback, A. De, T. DebRoy, Printability of alloys for additive manufacturing, Sci. Rep. 6 (2016) 19717, http://dx.doi.org/10.1038/srep19717.
[27] Y. Kakinuma, M. Mori, Y. Oda, T. Mori, M. Kashihara, A. Hansel, M. Fujishima, Influence of metal powder characteristics on product quality with directed energy deposition of Inconel 625, CIRP Ann. - Manuf. Technol. 65 (2016) 209–212, http://dx.doi.org/10.1016/j.cirp.2016.04.058.
[28] T.E. Abioye, J. Folkes, A.T. Clare, A parametric study of Inconel 625 wire laser deposition, J. Mater. Process. Technol. 213 (2013) 2145–2151, http://dx.doi.org/10.1016/j.jmatprotec.2013.06.007.
[29] E.R. Denlinger, J.C. Heigel, P. Michaleris, T.A. Palmer, Effect of inter-layer dwell time on distortion and residual stress in additive manufacturing of titanium and nickel alloys, J. Mater. Process. Tech. 215 (2015) 123–131, http://dx.doi.org/10.1016/j.jmatprotec.2014.07.030.
[30] C.P. Paul, P. Ganesh, S.K. Mishra, P. Bhargava, J. Negi, A.K. Nath, Investigating laser rapid manufacturing for Inconel-625 components, Opt. Laser Technol. (2007), http://dx.doi.org/10.1016/j.optlastec.2006.01.008.
[31] K. Amato, Comparison of microstructures and properties for a ni-base superalloy (alloy 625) fabricated by electron beam melting, J. Mater. Sci. Res. 1 (2012) p3, http://dx.doi.org/10.5539/jmsr.v1n2p3.
[32] Z. Wang, E. Denlinger, P. Michaleris, A.D. Stoica, D. Ma, A.M. Beese, Residual stress mapping in Inconel 625 fabricated through additive manufacturing: method for neutron diffraction measurements to validate thermomechanical model predictions, Mater. Des. 113 (2017), http://dx.doi.org/10.1016/j.matdes.2016.10.003.
[33] P. Ganesh, R. Kaul, C.P. Paul, P. Tiwari, S.K. Rai, R.C. Prasad, L.M. Kukreja, Fatigue and fracture toughness characteristics of laser rapid manufactured Inconel® 625 Structures, Mater. Sci. Eng. A. 527 (2010) 7490–7497, http://dx.doi.org/10.1016/j.msea.2010.08.034.
[34] N.H. Sateesh, G.C.M. Kumar, K. Prasad, S.C.K., A.R. Vinod, Microstructure and mechanical characterization of laser sintered inconel-625 superalloy, Procedia Mater. Sci. 5 (2014) 772–779, http://dx.doi.org/10.1016/j.mspro.2014.07.327.
[35] A. Kreitcberg, V. Brailovski, S. Turenne, Effect of heat treatment and hot isostatic pressing on the microstructure and mechanical properties of Inconel 625 alloy processed by laser powder bed fusion, Mater. Sci. Eng. A. 689 (2017) 1–10, http://dx.doi.org/10.1016/j.msea.2017.02.038.
[36] M. Sundararaman, P. Mukhopadhyay, S. Banerjee, Carbide precipitation in nickel base superalloys 718 and 625 and their effect on mechanical properties, TMS Superalloys 718 (1997) 367–378.
[37] T. Keller, G. Lindwall, S. Ghosh, L. Ma, B.M. Lane, F. Zhang, U.R. Kattner, E.A. Lass, J.C. Heigel, Y. Idell, M.E. Williams, A.J. Allen, J.E. Guyer, L.E. Levine, Application of finite element, phase-field, and CALPHAD-based methods to additive manufacturing of Ni-based superalloys, Acta Mater. 139 (2017) 244–253, http://dx.doi.org/10.1016/j.actamat.2017.05.003.
[38] C. Cortial, F. Corrieu, J. M, Vernot-Loier, Influence of heat treatment on microstructure, mechanical properties and corrosion resistance of weld alloy 625.pdf, Metall. Mater. Trans. a 26A (1995) 1273–1286, http://dx.doi.org/10.1007/BF02670621.
[39] V. Shankar, K. Bhanu Sankara Rao, S.L. Mannan, Microstructure and mechanical properties of Inconel 625 superalloy, J. Nucl. Mater. 288 (2001) 222–232, http://dx.doi.org/10.1016/S0022-3115(00)00723-6.
[40] B.K. Foster, A.M. Beese, J.S. Keist, E.T. McHale, T.A. Palmer, Impact of interlayer dwell time on microstructure and mechanical properties of nickel and titanium alloys, Metall. Mater. Trans. A. 48 (2017) 1–12, http://dx.doi.org/10.1007/s11661-017-4164-0.
[41] R. Tandon, T. Wilks, M. Gieseke, C. Noelke, S. Kaierle, T. Palmer, Additive Manufacturing of Elektron® 43 Alloy Using Laser Powder Bed and Directed Energy Deposition, Euro PM2015, 2015.
[42] A. B213, Standard test methods for flow rate of metal powders using the Hall flowmeter funnel, ASTM Int. i (2014) 213–216, http://dx.doi.org/10.1520/B0213-13.2.
[43] H.F. Funnel, Standard test method for apparent density of free-flowing metal powders using the Hall flowmeter funnel, ASTM Int. 2 (1999) 89–91, http://dx.doi.org/10.1520/B0212-13.2.
[44] International ASTM, Standard test method for tap density of metal powders and compounds, ASTM Int. (2015) 15–18, http://dx.doi.org/10.1520/B0527-15.2.
[45] A. C1444, Standard test method for measuring the angle of repose of free-flowing mold powders, ASTM Int (2000) 15–16, http://dx.doi.org/10.1520/C1444-00.
[46] J.S. Keist, T.A. Palmer, Role of geometry on properties of additively manufactured Ti-6Al-4V structures fabricated using laser based directed energy deposition, Mater. Des. 106 (2016) 482–494, http://dx.doi.org/10.1016/j.matdes.2016.05.045.
[47] J.J. Blecher, T.A. Palmer, T. Debroy, Solidification map of a nickel-base alloy, Metall. Mater. Trans. A Phys. Metall. Mater. Sci. 45 (2014) 2142–2151, http://dx.doi.org/10.1007/s11661-013-2149-1.
[48] Z. Wang, T.A. Palmer, A.M. Beese, Effect of processing parameters on microstructure and tensile properties of austenitic stainless steel 304L made by directed energy deposition additive manufacturing, Acta Mater. 110 (2016) 226–235, http://dx.doi.org/10.1016/j.actamat.2016.03.019.
[49] ASTM E8/E8M-15a, Standard test methods for tension testing of metallic materials 1, ASTM Int (2009) 1–27, http://dx.doi.org/10.1520/E0008.
[50] ASTM E646, Standard test method for tensile strain-hardening exponents (n-values) of metallic sheet materials, ASTM Int. 3 (2000) 1–8, http://dx.doi.org/10.1520/E0646-07E01.2.
[51] R. German, Powder Metallurgy and Particulate Material Processing, Metal Powder Industries Federation, Princeton, New Jersey, 2005, pp. 45–46-129.
[52] O.D. Neikov, D.V. Lotsko, V.G. Gopienko, Powder Characterization and Testing, Elsevier Ltd, 2009, http://dx.doi.org/10.1016/B978-1-85617-422-0.00001-X.
[53] X. Xue, L. Xu, Numerical simulation and prediction of solidification structure and mechanical property of a superalloy turbine blade, Mater. Sci. Eng. A 499 (2009) 69–73, http://dx.doi.org/10.1016/j.msea.2007.12.052.